Computational Fluid Dynamics Analysis and Optimisation of Polymerase Chain Reaction Thermal Flow Systems

Hazim S. Hamad[a,b,*], N. Kapur[b], Z. Khatir[c], O.M. Querin[b], H.M. Thompson[b], Yongxing Wang[b], M.C.T. Wilson[b]

[a]*Ministry of oil, Iraq*
[b]*School of Mechanical Engineering, University of Leeds, Leeds, UK.*
[c]*Birmingham City University, UK.*

Abstract

A novel Computational Fluid Dynamics-enabled multi-objective optimisation methodology for Polymerase Chain Reaction flow systems is proposed and used to explore the effect of geometry, material and flow variables on the temperature uniformity, pressure drop and heating power requirements, in a prototype three-zone thermal flow system. A conjugate heat transfer model for the three-dimensional flow and heat transfer is developed and solved numerically using COMSOL Multiphysics® and the solutions obtained demonstrate how the design variables affect each of the three performance parameters. These show that choosing a substrate with high conductivity and small thickness, together with a small channel area, generally improves the temperature uniformity in each zone, while channel area and substrate conductivity have the key influences on pressure drop and heating power respectively. The multi-objective optimisation methodology employs accurate surrogate modelling facilitated by Machine Learning via fully-connected Neural Networks to create Pareto curves which demonstrate clearly the compromises that can be struck between temperature uniformity throughout the three zones and the pressure drop and heating power required.

Keywords: PCR, Computational Fluid Dynamics, Machine Learning, Multi-Objective Optimisation.

*Corresponding author
Email address:* `mnhsh@leeds.ac.uk` (Hazim S. Hamad)

Nomenclature

A   area (m^2)
Bi biot number
C_p constant-pressure specific heat
D_h hydraulic diameter (mm)
H microchannel height (mm)
h Heat transfer coefficient $[W/m^2.K]$
k thermal conductivity $(W/m.K)$
L length (mm)
$\dot{m}$ mass flow rate (kg/s)
N_u Nusselt number
P microchannel perimeter (mm)
Δp pressure drop (Pa)
Pe Peclet number , $V_{ch}D_h/\alpha$
Pr Prandtl number
q wall heat flux (W/m^2)
Q total power generated by PCR chip (W)
R_{th} conduction thermal resistance (K/W)
Re Reynolds number , $Re = \rho V_{ch}D_h/\mu$
S spacing between heaters (mm)
T temperature (K)
V velocity (mm/s)
$\dot{V}$ volumetric flow rate (m^3/s)
W width

Subscripts

avg average
b substrate
c channel
CFD computational fluid dynamics
dev deviation
FEM finite element method
f fluid
h heater
in inlet
max maximum
min minimum
out outlet
$RMSE$ root-mean-square error
s solid
w wall

Greek symbols

2

α thermal diffusivity
Δ drop
ρ density (kg/m^3)
μ dynamic viscosity $(Pa.s)$
ν kinematic viscosity (m^2/s)

1. Introduction

Precise thermal control during the processing of small volumes of liquid in arrays of fluidic channels is a key enabling technology for numerous important applications. These include chemical reactors, fuel and solar cells, pharmaceuticals and droplet freezing systems to determine environmental pollution levels [1, 2]. In the context of electronics cooling, the increasing densities of integrated circuits (up to $10kW/cm^2$ by 2020 [3]) have inspired significant recent research interest in single phase liquid flows in fluidic channels as a viable and practical method for cooling high heat flux densities encountered e.g. in Radio Frequency and microwave applications [4]. Single-phase flow in serpentine channels has recently been shown to be particularly well-suited to providing uniform processor temperatures for high density electronics cooling applications [5].

This paper is concerned with the thermo-flow design and optimisation of fluidic channels used in Polymerase Chain Reaction (PCR) systems. Since their introduction, PCR systems have revolutionised biological research [6]. They have found widespread application in rapid diagnostic systems for bacterial species leading to e.g. infectious diseases, or for the rapid and accurate detection of bacterial species causing micro-biologically induced corrosion in oil and gas production systems [7, 8]. PCR systems perform a thermal cycling procedure which incorporates three distinct stages of denaturation (melting of the double-stranded DNA at $\sim 95°C$), annealing (binding of the specific primers of the thermo-stable DNA polymerase between $40°C \sim 50°C$) and extension (extending the primers within the thermo-stable DNA at $60°C \sim 70°C$) [9].

Early PCR systems used time-consuming devices involving wells where the whole chip is heated up and cooled down during each thermal stage [10, 11]. These were superseded by Continuous Flow PCR (CFPCR) devices, introduced first by [12], based on single phase flow in a serpentine fluidic channel of rectangular cross-section with three temperature stages in a glass substrate supported by three independent copper block heaters, see Figure 1. Several studies show that, when used in a serpentine arrangement, CFPCR offers reduced reagent consumption and rapid heat transfer, enabling PCR processing times to be reduced dramatically compared to well-based systems. Due to their potential to provide an isolated environment with lower thermal mass than single-phase systems, there are now intensive efforts to create droplet-based PCR systems [6, 10]. However, currently most practical systems use CFPCR based on single-phase flow and these are the focus of the present study. Previous studies of these have shown that the most influential parameters include the substrate's thermal conductivity and the system's thermal resistance, and that fluidic channel sizes and spacing, carrier heat capacity and flow rate and, crucially, the heating arrangement chosen are also all very influential [13].

Controlling the residence times in the denaturation, annealing and extension zones is crucial since insufficient dwell times in each thermal state can seriously degrade DNA amplification efficiency[14]. Residence times in each zone can be optimised by controlling flow rate and channel geometry [15]. Cao et al. [16] explored the role of absolute and relative residence times on DNA amplification efficiency using a combined experimental and numerical approach. The latter employed a Lagrangian modelling approach to predict the temperature

3

histories of individual DNA molecules flowing through CFPCR devices. Their methodology

45 enabled design times for CFPCR devices to be reduced significantly. A number of other studies have shown that it is also important to control the interference and transition times between the thermal zones, which may require the use of active heating and cooling between the zones, since ordering and interactions between the PCR thermal zones affects PCR yield significantly. These considerations complicate the drive towards CFPCR device miniatur-

50 isation, to develop portable devices for diagnostic and testing purposes, since minimising thermal interference between neighbouring serpentine channels tends to lead to wider fluidic devices [14].

The geometry of the serpentine channels is very important and a number of studies have attempted to improve PCR yield by providing a more uniform thermo-flow environment

55 within the PCR zones. Reference [17], for example, used spiral microchannels to reduce reaction times, while other studies have explored the benefits of employing radial [18], spiral [19] and straight channels [20, 21]. Duryodhan et al [22] showed how diverging fluidic channels can create more uniform wall temperatures as a first step to improving the overall temperature uniformity of fluid flowing within the PCR zones. Improved flow uniformity

60 was also achieved through use of electro-kinetic flow to create a plug-like velocity profile to reduce sample dispersion and increase flow-rate control within PCR channels [23].

Selecting appropriate thermal properties which are biologically compatible with the PCR liquid [24], is also very important for CFPCR device optimisation [25], and the goal of minimising the heating power required [26]. Tsuda et al. [27] demonstrated the ability

65 of 3D printing to produce bespoke fluidic reactors with complete control of the 3D fluidic network, a finding which motivated a recent exploration of the potential of using 3D printed serpentine fluidic channels for CFPCR [9]. The flexibility of 3D printing allowed them to explore a number of alternative heating arrangements with heaters located under each of the three temperature zones. They noted that the low thermal conductivity of the 3D printable

70 materials is an important factor limiting their application in CFPCR devices that require rapid heating and cooling.

The above review demonstrates that there remains ample scope for CFPCR device optimisation. The present study proposes a novel Computational Fluid Dynamics (CFD)-enabled optimisation methodology which enables the trade-offs between competing objec-

75 tives of temperature uniformity, pressure drop and heating power consumption to be explored. This allows designers to maximise the proportion of PCR liquid that experiences the target temperature range for the required time period in each zone, to preserve the structural integrity of the CFPCR chip or to minimise the time taken or overall power consumption (heating and hydraulic) throughout thermal cycling.

80 The paper is organised as follows. Section 2 describes the numerical methods and the specification of the conjugate heat transfer problem. Section 3 presents the validation of the numerical model and a series of numerical results which demonstrate the dependence of the thermal flow systems on key parameters. Section 4 presents a multi-objective optimisation formulation for PCR flows and a series of CFD and optimisation results which demonstrate

85 the potential to manipulate designs to achieve the competing objectives. Finally, conclusions are drawn in Section 5.
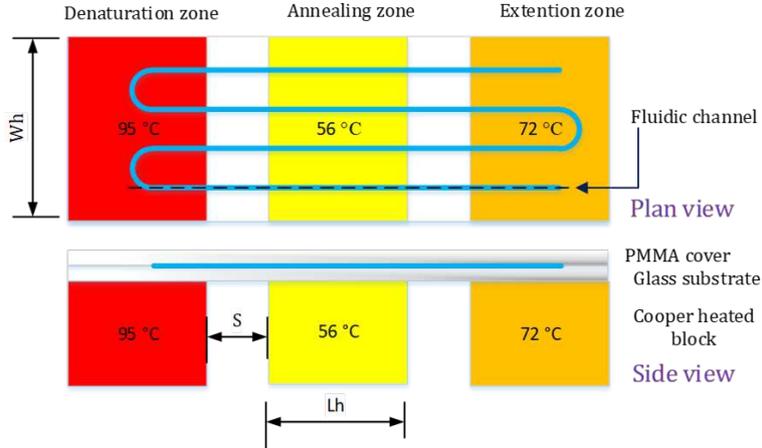
4

Figure 1: Serpentine PCR systems.

2. Numerical Methods

The problem of the microfluidic channel and heating arrangements, together with modelling and numerical methods are described in this section.

2.1. Problem Description and Configuration

The serpentine microfluidic channel, shown in Figure 1, passing through denaturation ($95°C$), annealing ($56°C$) and extension ($72°C$) zones is used as a prototypical CFPCR thermal flow problem. This is based on those considered previously by [14, 17, 28] but with a glass, rather than a PDMS, substrate material to increase thermal conductivity and temperature uniformity. In addition, the cover material (H_p) used here is PMMA, which can provide good thermal insulation as well as the practical advantages of good optical access and a low cost. A schematic diagram of the microfluidic channel geometry is presented in Figure 2 where W_c, H_c, W_w, H_b and L are the microchannel width, height, wall thickness (the space between the channels), the bottom height and the total length respectively.

There are three individual copper blocks with cartridge heaters placed underneath the glass chip with a constant distance between them of $S = 1mm$, the length of the heaters being $9mm$ underneath the denaturation and annealing zones and $40mm$ underneath the extension zone. The height and length of each heater are $H_h = 2mm$ and $L_h = 9mm$. The length of the denaturation, annealing and extension zones are chosen to achieve the typical residence time ratios of $1 : 1 : 4$ respectively [28].

2.2. Conjugate Heat Transfer Model

A conjugate heat transfer model of the steady, single-phase, laminar flow problem shown in Figure 2 was developed using the following simplifying assumptions employed by previous studies [28–31]. The liquid is water, with temperature-dependent density and viscosity, and the effects of radiation and buoyancy are neglected within the computational domain. However, the upper surface of the domain includes the effect of natural convection via a heat
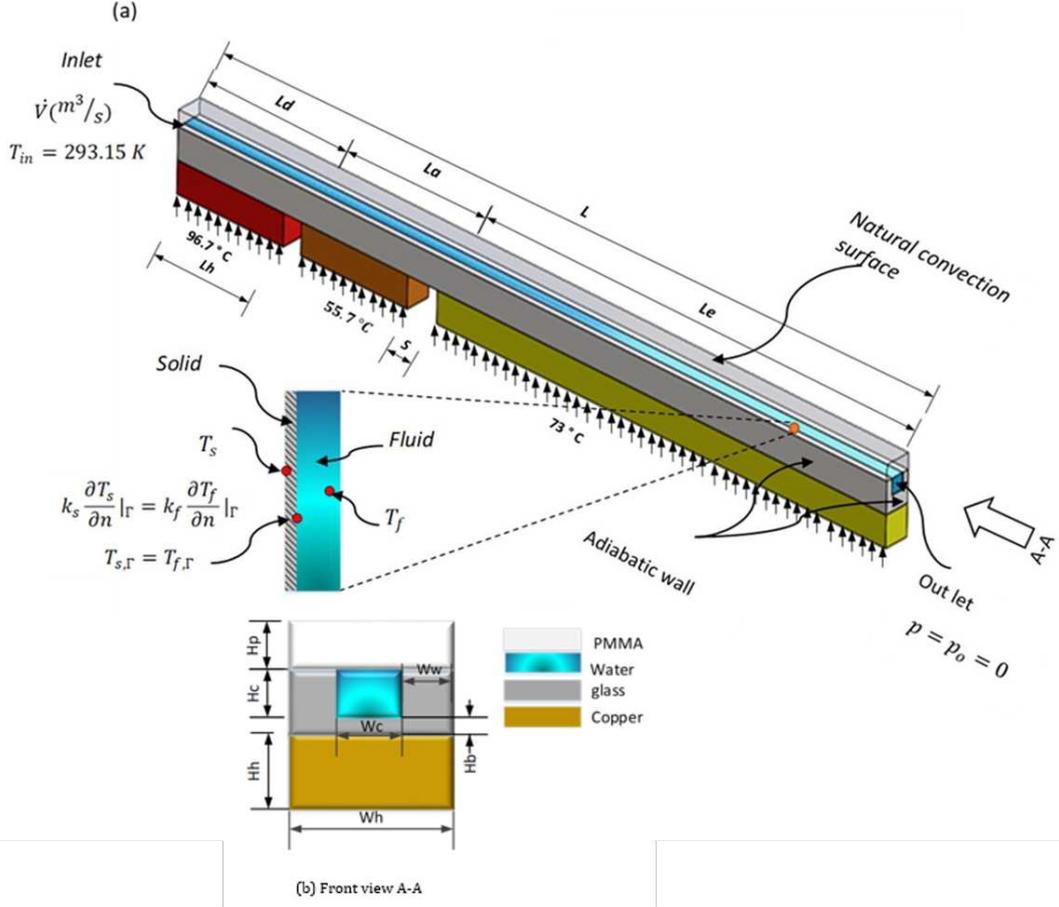
5

Figure 2: A schematic diagram of the microfluidic channel and heating arrangements in each of the CFPCR zones: a) the thermal boundary conditions applied in each zone and b) the cross-section of the microfluidic channel.

transfer coefficient of $15 W/(m^2 \cdot K)$ [28, 32]. All other surfaces are taken to be adiabatic except at the channel bottom (where the heat flux or wall temperature boundary conditions are applied). There is no internal heat generation.

The Reynolds number (Re), is given by:

$$Re = \frac{\rho_f V_{ch} D_h}{\mu_f}, \tag{1}$$

where ρ_f and μ_f are the density and viscosity of the fluid respectively, V_{ch} is the channel inlet velocity and D_h the channel hydraulic diameter defined by:

$$D_h = \frac{2 W_c H_c}{W_c + H_c}. \tag{2}$$

For CFPCR flows, $V_{ch} \sim 1 mm/s$, $D_h \sim 10^{-4}$ m and a water density of $10^3 kg/m^3$ and dynamic viscosity $10^{-3} Pa \cdot s$, leads to $Re \sim O(10^{-1})$, i.e. laminar flow conditions.

This is modelled using the governing continuity and Navier–Stokes equations:

$$\nabla \cdot (\rho_f \mathbf{u}) = 0, \tag{3}$$

6

and

$$\rho_f(T) \left(\mathbf{u} \cdot \nabla \right) \mathbf{u} + \nabla \cdot \left[\mu_f \left(T \right) \left(\nabla \mathbf{u} + \nabla^T \mathbf{u} \right) - p\mathbf{I} - \frac{2}{3} \mu_f \left(T \right) \nabla \cdot \mathbf{u}\mathbf{I} \right] = 0, \qquad (4)$$

where $\mathbf{u}$ and p are respectively the fluid velocity vector and pressure. The energy equations for the heat transfer in the fluid and solid can be expressed respectively as:

$$\rho_f(T_f)C_{pf}\left(T_f \right) \mathbf{u} \cdot \nabla T_f = \nabla \cdot \left(k_f \nabla T_f \right) + \dot{Q}_{gen}, \qquad (5)$$

and

$$\nabla \cdot \left(k_s \nabla T_s \right) = 0, \qquad (6)$$

where C_{pf}, k_f and k_s represent the specific heat and thermal conductivities of the fluid and solid respectively. $\dot{Q}_{gen}$ denotes the internal heat generation (W/m^3) which is taken to be 0.

2.3. Boundary Conditions

The computational domain and boundary conditions are shown in Figure 2. At the walls, no-slip velocity boundary conditions $\mathbf{u} = \mathbf{u}_s = 0$ and wall temperatures $T_f = T_s$ are imposed, where T_f and T_s are respectively the interface temperature for the fluid and the solid. At fluid-solid boundaries heat flux continuity is imposed. The inlet velocity V_{ch} was set to achieve a typical Reynolds number of 0.7 and the inlet temperature was fixed at $T_{f,in} = 20°C$, with an ambient pressure condition, $p = p_0$, imposed at the outlet.

All the outer surface boundary conditions are considered to be adiabatic except at the bottom of the copper heaters where temperatures are set to 96.7°C, 73°C and 55.7°C respectively for the denaturation, extension and annealing zones. The thermo-physical properties of the water (ρ_f, μ_f, C_{pf} and k_f) depend on the temperature and are given by [33]:

$$\rho_f = 838.466 + 1.4T - 0.003T^2 + 3.72 \times 10^{-7}T^3, \qquad (7)$$

$$\begin{aligned} \mu_f =\,&1.38 - 0.0212T - 1.36 \times 10^{-4}T^2 - 4.64 \times 10^{-7}T^3 \\ &+ 8.9 \times 10^{-10}T^4 - 9.08 \times 10^{-13}T^5 + 3.846 \times 10^{-16}T^6, \end{aligned} \qquad (8)$$

$$C_{pf} = 12010.147 - 80.407T + 0.3099T^2 - 5.382 \times 10^{-4}T^3 + 3.625 \times 10^{-7}T^4, \qquad (9)$$

$$k_f = -0.869 + 0.00895T - 1.584 \times 10^{-4}T^2 - 7.975 \times 10^{-9}T^3, \qquad (10)$$

where T is in Kelvin. The thermal conductivity of copper is $k_s = 400W/(m \cdot K)$ and the target temperatures in the denaturation, annealing and extension zones are (95°C, 55°C and 72°C) respectively. The governing equations are solved subject to the boundary conditions using COMSOL Multiphysics 5.4. The temperature uniformity in the zones is calculated by quantifying deviations from the target temperature, T_{target}, via

$$T_{dev} = \sqrt{\frac{\iiint \left(T_{f_{i,j,k}} - T_{target} \right)^2 dV}{\iiint dV}}. \qquad (11)$$

7

The hydraulic performance is measured by calculating the pressure difference along the channel

$$\Delta p = p_{in} - p_{out}. \tag{12}$$

Heating power, Q, in each zone Q_d, Q_e and Q_a was obtained at the bottom of the heater surfaces using $\mathbf{n} \cdot (k\nabla T) = q/A_h$ where $\mathbf{n}$ denotes the outward normal vector of the domain and A_h is the surface area of the heater. The total heat power is calculated by:

$$Q_t = Q_d + Q_a + Q_e, \tag{13}$$

where Q_t, Q_d, Q_a and Q_e represent the total heat power in watts (W), heat transfer to denaturation zone, and heat extracted from annealing zone and heat transfer to the extension zone respectively.

3. Numerical Results

3.1. Numerical Validation

The effect of grid density is examined by obtaining numerical solutions on a series of structured Finite Element grids of increasing refinement, on a desktop PC with Microsoft Windows 10 and 32GB physical RAM. Table 1 shows the number of degrees of freedom (DOF), physical memory (PM), Virtual Memory (VM), execution time and calculated T_{dev} and Δp for each grid. There is only a small change $< 0.2\%$ in the obtained results if the number of mesh elements is increased above 877552. Accordingly, numerical results presented below have been obtained on the mesh with 877552 elements as an appropriate compromise between computational expense and accuracy.

NO. of elements	DOF ($\times 10^5$)	PM (GB)	VM (GB)	Time	$\Delta p(Pa)$	T_{dev}
93024	2.52	2.71	3.28	119	51.31	27.98
216096	5.1679	3.17	3.92	303	51.00	27.81
380480	8.3090	3.89	4.67	553	50.64	27.70
448686	14.485	4.47	5.26	677	50.58	27.58
877552	17.763	6.56	7.42	1839	50.48	27.57
1026602	20.373	8.23	9.52	3849	50.45	27.50
1171632	23.329	7.93	8.92	4050	50.43	27.52

Table 1: Effect of grid density for the case of $Re = 0.7$, $T_f = 20°C$, $H_c = 150\mu m$, $W_c = 500\mu m$, $W_w = 150\mu m$ and $H_b = 850\mu m$.

The numerical model is first compared with the experimental results of [22] for thermal flow in diverging channels. Figure 3 shows that the agreement between the experimental and numerical results is generally very good. The next comparison is with the numerical results of [28] where $H_c = 150\mu m$, $W_c = 50\mu m$, $S = 1mm$, $V_{ch} = 6mm/s$ and $T_{f,in} = 72°C$. Once again the numerical predictions of the temperature profile along the three temperature zones, shown in Figure 4, are in very good agreement with the published results.
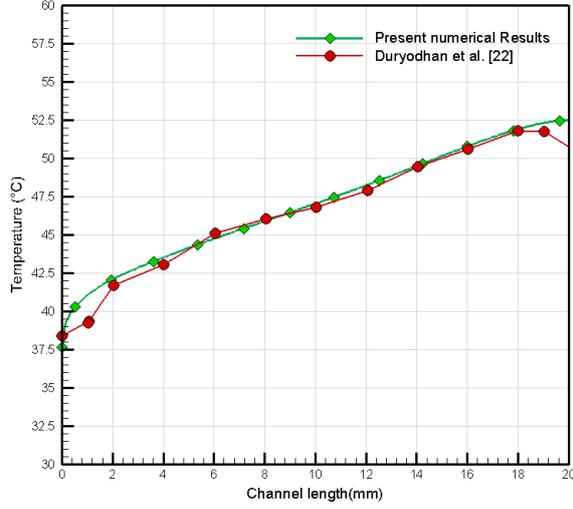
8

Figure 3: Comparison of surface temperature variation along flow direction in a diverging microchannel at $q = 4W$.
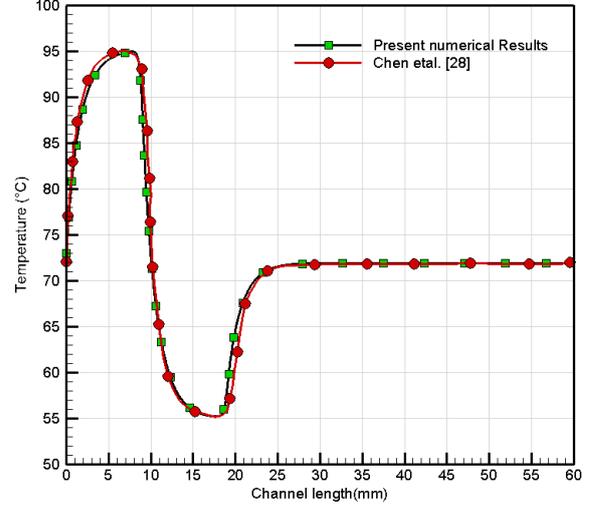
Figure 4: Comparison of fluid average temperature profile along the centreline of CFPCR zones.

3.2. One-dimensional (1-D) thermal modelling

Several previous studies of heat transfer in micro-channel structures have employed simplified analyses successfully. For small channels with $D_h \sim 50\mu m$, convective heat transfer can often be neglected [23] and for flows which are fully developed thermally, 1-D models may also be useful. The thermal entrance length for laminar flow can be estimated by [34]

$$L_{th} = 0.05 RePrD_h \tag{14}$$

where Pr is the Prandtl number given by

$$Pr = \frac{C_p \mu}{k}. \tag{15}$$

For the cases considered here $L_{th} \sim 20\mu$m so the thermal entrance length can be neglected. By applying the energy balance approach described in [33, 35] the average flow temperature, $T_{f,avg}$, for the constant wall temperature, T_w, is given by

$$T_{f,avg}(x) = T_w - (T_w - T_{in}) \times \exp(-h.P.x/\dot{m}C_{pf}) \tag{16}$$

where x is the distance along the channel, T_{in} is the fluid inlet temperature, $\dot{m}$ is the mass flow rate, h is the heat transfer coefficient, P is the perimeter of the microchannel and C_{pf} is the fluid heat capacity.

Predictions of the 1-D model (16) are compared with those of the 3-D conjugate heat transfer model in Figure 5, for the thermal conditions specified in the denaturation zone. Figure 5(a) shows that for the case with V_{ch}=4mm/s and zero substrate thickness, $H_b = 0\mu m$, the agreement is excellent. However for cases with larger values of H_b, the discrepancy

9

between the models is much more significant due to the thermal resistance of the substrate. More generally, it is found that the 1-D model works well provided the conductive thermal resistance, defined by $R_{th} = H_b/k_s$, is small. This cannot be neglected for cases considered below, with larger substrate thicknesses, and for which full 3-D simulations are required.
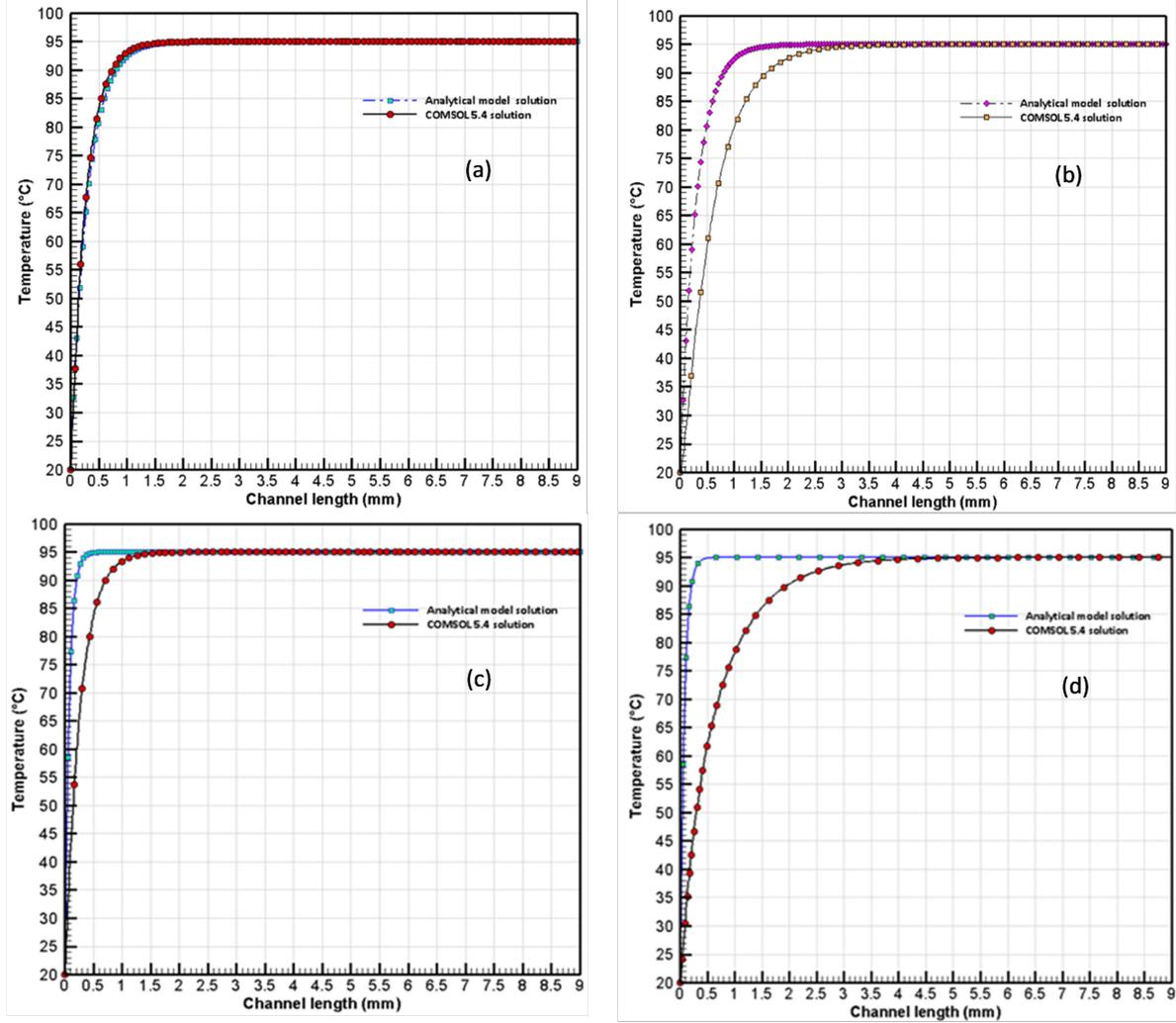

Figure 5: Comparison of 1-D and CFD predictions of centreline temperature in the CFPCR denaturation zone with (a) V_{ch}=4mm/s, H_b=0 μm; (b) V_{ch}=4mm/s, H_b=200μm; (c) V_{ch}=1mm/s, H_b=200μm; (d) V_{ch}=1mm/s, H_b=850μm

3.3. Effect of substrate material

The effect of the substrate material on the temperature profile is considered next, for flow in a channel with dimensions: $H_c = 150\mu m$, $W_c = 500\mu m$, $H_b = 850\mu m$, $W_w = 50\mu m$, $H_h = 2000\mu m$, $H_{PMMA} = 1500\mu m$ and $S = 1mm$. Figure 6 shows the effect of the material on the fluid temperature profile at the low inlet flow velocity $V_{ch} = 0.1mm/s$.

10

The fluid temperatures in these cases are reasonably uniform for all materials, with the fluid temperature for glass and silicone chips being closest to the target temperatures in the zones while that for the polyimide chip is furthest from the target profile. The size of the deviations from the target temperature profiles generally decreases as the thermal conductivity of the chip material increases due to the smaller thermal resistance between the heated substrate and the flowing liquid. As noted by Chen et al. [14], this can however lead to greater thermal interference between zones.
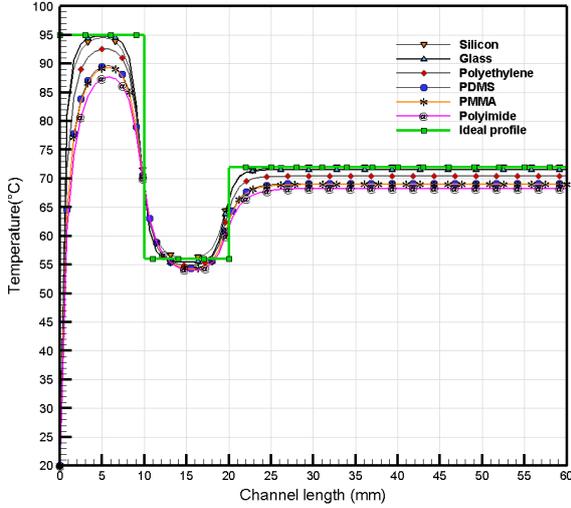

Figure 6: Temperature profile along the centerline of CFPCR zones at $V_{ch} = 0.1mm/s$.
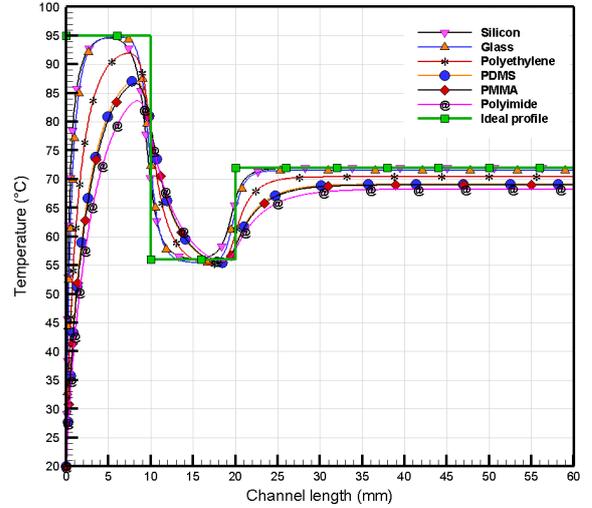

Figure 7: Temperature profile along the centerline of CFPCR zones at $V_{ch} = 1mm/s$.

Figure 7 shows the effect of increasing the inlet velocity to $V_{ch} = 1mm/s$. This leads to greater discrepancies from the target temperatures in each zone, since convective heat transfer becomes more significant at the higher speed. Once again, the deviations from the target temperature profile decrease as thermal conductivity increases. Figure 8 summarises the effect of material and inlet flow velocity on the deviations from the target temperatures, and quantifies the monotonic increases in T_{dev} as V_{ch} increases and thermal conductivity decreases, due to the increased convection and thermal resistance respectively.

It is instructive to calculate two dimensionless parameters for the present problems. The first, the Peclet number, quantifies the relative importance of convection compared to conduction in the liquid and is defined by Lin et al. [36]:

$$P_e = V_{ch}.D_h/\alpha \tag{17}$$

where α is the thermal diffusivity of the liquid. The second assesses the importance of axial conduction compared to convection in micro-scale systems and is defined by Maranzana et al. [37]:

$$M = q_{cond}/q_{conv} = (k_s.H_b)/(\rho_f.C_{pf}.H_c.V_{ch}) \tag{18}$$

11

Material	T_{dev} (°C)			P_e			M		
	V_{ch1}	V_{ch2}	V_{ch3}	V_{ch1}	V_{ch2}	V_{ch3}	V_{ch1}	V_{ch2}	V_{ch3}
Polyimide	44.522	73.888	94.613	1.442	8.850	14.978	0.0034	5.81×10^{-4}	3.49×10^{-4}
PMMA	40.336	63.988	84.747	1.439	8.794	14.858	0.0044	7.35×10^{-4}	4.41×10^{-4}
PDMS	39.448	62.881	82.573	1.439	8.783	14.834	0.00463	7.74×10^{-4}	5.36×10^{-4}
Polyethylene	29.665	57.753	61.778	1.434	8.679	14.583	0.0088	0.00148	8.82×10^{-4}
Glass	19.366	38.309	47.790	1.430	8.597	14.359	0.0324	0.0054	0.0032
Silicon	18.152	20.799	22.922	1.428	8.575	14.295	3.0129	0.502	0.301

Table 2: The effect of chip material and inlet velocity on T_{dev}, Pe and M for $V_{ch1} = 1mm/s$, $V_{ch2} = 6mm/s$, $V_{ch3} = 10mm/s$, for $H_b = 850\mu m$.

Values are given in Table 2 for examples of the cases considered here.

Since $Pe > 1$ convection is influential in all cases and temperature variations along the channel result from the competition between convection, which acts to increase them, and conduction, which acts to reduce them. Lower axial conduction for the particular case of PMMA at V_{ch}=1mm/s may explain why its $T_{dev} = 40.336$ is greater than $T_{dev} = 38.309$ for glass at the much higher velocity V_{ch}=6mm/s.

In view of its good thermal and optical properties, all results below use glass as the substrate material. Figure 9 and Table 2 show how the temperature variation T_{dev} in glass chips is affected by channel inlet velocity V_{ch} and demonstrates clearly how the temperature profile throughout the three PCR zones is very different from the target profile at the higher speeds.

Material	$Q_t(W)$				
	$k_s(W/m.K)$	V_{ch1}	V_{ch2}	V_{ch3}	V_{ch4}
Polyimide	0.15	0.054	0.105	0.146	0.183
PMMA	0.19	0.058	0.109	0.157	0.203
PDMS	0.2	0.059	0.111	0.160	0.207
Polyethylene	0.38	0.071	0.164	0.195	0.246
Glass	1.4	0.122	0.283	0.393	0.475
Silicon	130	5.293	5.384	5.476	5.607

Table 3: The effect of chip material on heating power required for $V_{ch1} = 1mm/s$, $V_{ch2} = 6mm/s$, $V_{ch3} = 10mm/s$, $V_{ch4} = 15mm/s$.

The effect on heating power is considered next. Figure 10 and Table 3 show that the heating power consumption increases as the velocity increases and that the comparatively high thermal conductivity of silicon leads to at least an order of magnitude larger heating power requirement.

The results show that T_{dev} is influenced by the competition between convection and axial conduction that results from the material type, flow rate and channel size. In practice, there are other competing objectives which need to be considered, such as the need to minimise
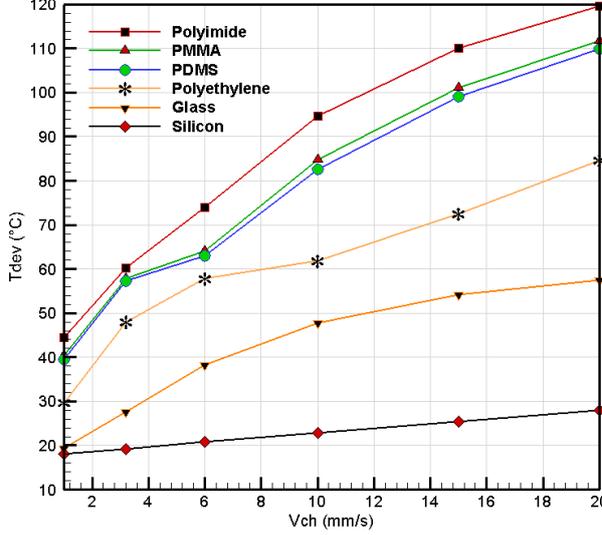
Figure 8: The effect of material type on the PCR performance responses in terms of T_{dev} at different inlet velocity $V_{ch} = (1 - 20)mm/s$.
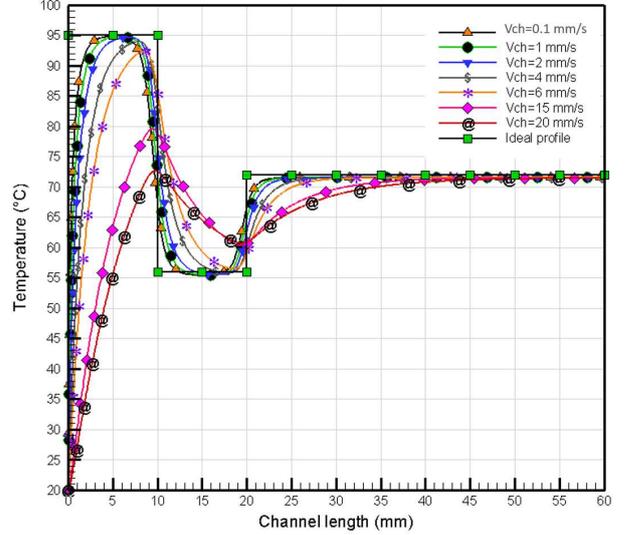
Figure 9: Temperature profile along the centerline of CFPCR zones at different velocities using a glass substrate.

the pressure drop and heating power consumption. The next section extends the analysis to formulate and solve multi-objective optimisation problems relevant to PCR systems.

4. Multi-Objective Optimisation

4.1. Problem Formulation

The prototype three-zone PCR system is optimised according to the competing objectives of minimising each of the temperature deviation, T_{dev}, pressure drop, Δp, and heating power, Q_t. The influence of the four design variables W_c, H_c, H_b and W_w is explored at a constant Reynolds number $Re = 0.7$, and with constant $T_{f,in} = 20°C$, $S = 1mm$, $H_h = 2mm$, $H_p = 1.5mm$ and $L = 60mm$. Temperatures at the bottom of the copper heaters over the denaturation, extension and annealing zones are set at $96.7°C$, $73°C$ and $55.76°C$ respectively. The multi-objective optimisation problem considered here is the minimisation of each of $\{T_{dev}, \Delta p, Q_t\}$ within the design space:

$$150\mu m \leq W_c \leq 500\mu m, 50\mu m \leq H_c \leq 150\mu m, 400\mu m \leq H_b \leq 1000\mu m, 70\mu m \leq W_w \leq 1000\mu m.$$

4.2. Effect of channel size

Table 4 shows typical results of varying the channel dimensions, W_c and H_c, on the pressure drop Δp and temperature deviation T_{dev}. Pressure drop Δp is effectively independent of H_b and W_w and depends only on the W_c and H_c through a strong dependence on channel cross-sectional area, $W_c \times H_c$. In contrast, T_{dev} also depends on H_b through its influence on the substrate thermal resistance. As H_b increases, conduction into the liquid decreases leading to larger temperature variations.
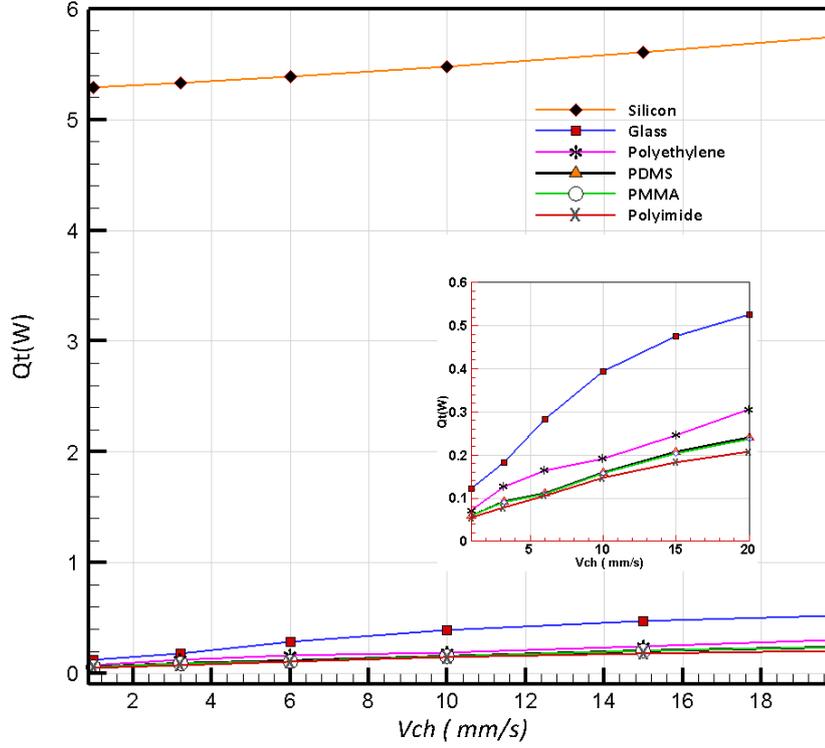
13

Figure 10: The effect of material type and inlet velocity V_{ch} on the heating power requirement.

Case no.	W_c(mm)	H_c (mm)	H_b(mm)	$\Delta p(Pa)$	$T_{dev}(K)$
1	0.5	0.15	0.8	50.27	26.04
2	0.5	0.05	0.8	993.62	22.52
3	0.15	0.15	0.8	147.59	25.74
4	0.15	0.05	0.8	1416.10	20.44
5	0.5	0.15	0.4	49.92	19.71
6	0.5	0.05	0.4	986.33	16.66
7	0.15	0.15	0.4	146.67	19.34
8	0.15	0.05	0.4	1413.30	15.30

Table 4: Effect of channel size on T_{dev} and Δp for the case of $Re = 0.7$, $T_f = 20°C$, $W_w = 0.07$mm.

4.3. Surrogate Modelling

Design of Experiments (DoE) using an Optimal Latin Hyper-cube sampling technique [38], and CFD simulations run at these design points was used to generate the $\mathbf{y} = (T_{dev}, \Delta p, Q_t)$ data set for use within surrogate models. Two surrogate modelling approaches are used. The first is based on cubic Radial Basis Functions (RBFs) where the surrogate model y_k (k^{th} component of $\mathbf{y}$ with $k = 1, 2, 3$) for the output variable $\mathbf{y}$ at a design point $\mathbf{x} = (W_c, H_c, H_b, W_w)$

14

is given by

$$y_k(\mathbf{x}) = \sum_{i=1}^{N} \lambda_i \phi\left(\|\mathbf{x} - \mathbf{x}_i\|\right), \quad \phi\left(\|\mathbf{x} - \mathbf{x}_i\|\right) = \beta\|\mathbf{x} - \mathbf{x}_i\|^3, \tag{19}$$

with $\mathbf{x}_i$ being the ith DoE point $(1 \leq i \leq N)$, taken from $N = 560$ CFD simulations. $\|\cdot\|$ denotes the l^2 norm, λ_i are RBF parameters. β is a calibration parameter for the cubic RBF function. For each surrogate model β is determined using a relatively simple Leave-One-Out (LOO) calibration, where each sample point is left out of the RBF function and then used to predict the value at the omitted DoE point. The Root Mean Square Error (RMSE) of the discrepancies between the predicted and actual DoE points is then minimised with respect to the β parameter over a suitable interval [39].

The second approach uses fully connected Neural Networks (NNs) available within Tensor Flow, using N_{train}=176 of these randomly selected for the training data set and the remaining N_{tests}=50 used as the test data set. A Stochastic Gradient Descent (SGD) method is used to minimise the cost function:

$$cost = \sum_{i=1}^{N_{train}} \|\mathbf{y}_i^{predict} - \bar{\mathbf{y}}_i^{train}\|/N_{train}. \tag{20}$$

The calculations are terminated after 5×10^4 iterations to avoid over-fitting when the error

$$err = \sum_{i=1}^{N_{train}} \|\mathbf{y}_i^{predict} - \bar{\mathbf{y}}_i^{test}\|/N_{test} \tag{21}$$

does not decrease as shown in Figure 11.

In (20) and (21), $\bar{\mathbf{y}}$ is the normalised data set given by

$$\bar{y}_k = \frac{y_k - y_{k,min}}{y_{k,max} - y_{k,min}}, \quad (k = 1, 2, 3) \tag{22}$$

with y_k being the kth component of $\mathbf{y}$, and $y_{k,min}$ ($y_{k,max}$) being the minimum (maximum) of all the N data points for the kth component.

The training procedure random process is performed 10 times for the same NN before the effect of using different topologies is explored. The three best NNs that can reduce the error in the testing dataset to around 0.3% are shown in Figure 12.

A reliable method of determining the best NN is to let them predict another unseen data set. Therefore these three NNs are tested on 50 additional CFD data points, and the relative error is shown in Table 5. From these we can conclude that the one-layer NN with 100 neurons is the most accurate, and will be used in all NN results presented below.

4.4. Multi-Objective Pareto Analysis

The RBF and NN methods were used to create Pareto curves of non-dominated solutions for Δp vs T_{dev}, Δp vs Q_t and T_{dev} vs Q_t. The RBF method uses the Multi-Objective Genetic Algorithm (MOGA) solver in MATLAB, whereas the NN methods use
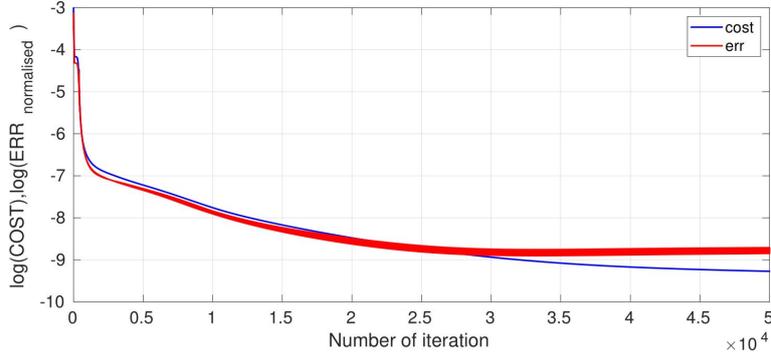
Figure 11: Convergence of the cost function evaluated on the training data and error measured on the test data set.
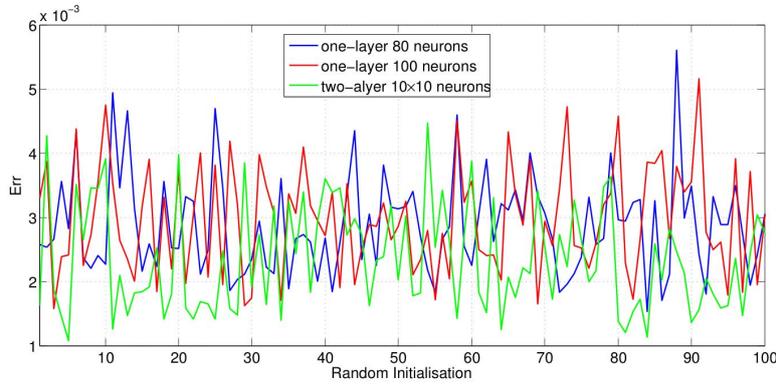

Figure 12: Final error of running the same NN 100 times, which is initialized randomly.

One-layer NN with 80 neurons	one-layer NN with 100 neurons	Two-layer NN with 10×10 neurons
3.5773×10^{-3}	2.0128×10^{-3}	2.4820×10^{-3}

Table 5: Error testing on 50 additional data points.

the SciPy.optimization module in Python based on a simple weighting between the competing objectives. The Pareto curves from the RBF and NN meta-modelling are all very similar to each other - the Pareto curves for Δp vs T_{dev} are shown in Figure 13 and provide a basis for finding an appropriate balance between these competing objectives. It shows, for example, that reducing T_{dev} from 14 to 13 would require a four-fold increase of Δp, from 250 to $1000Pa$, while reducing Δp below $100Pa$ comes at the price of a sharp rise in T_{dev}.

Figure 14 compares the temperature profile from a design point on the Pareto curve ($H_c = 50\mu m$, $W_c = 152\mu m$, $H_b = 403\mu m$, $W_w = 667\mu m$, $H_h = 2000\mu m$, $H_{PMMA} = 1500\mu m$ and $S = 1mm$) with that from a non-optimised Design of Experiments point ($H_c = 150\mu m$, $W_c = 500\mu m$, $H_b = 800\mu m$, $W_w = 70\mu m$, $H_h = 2000\mu m$, $H_{PMMA} = 1500\mu m$ and $S = 1mm$). It can be seen that the temperature profile from the optimised solution is much closer to the target temperature profile than for the non-optimised one.
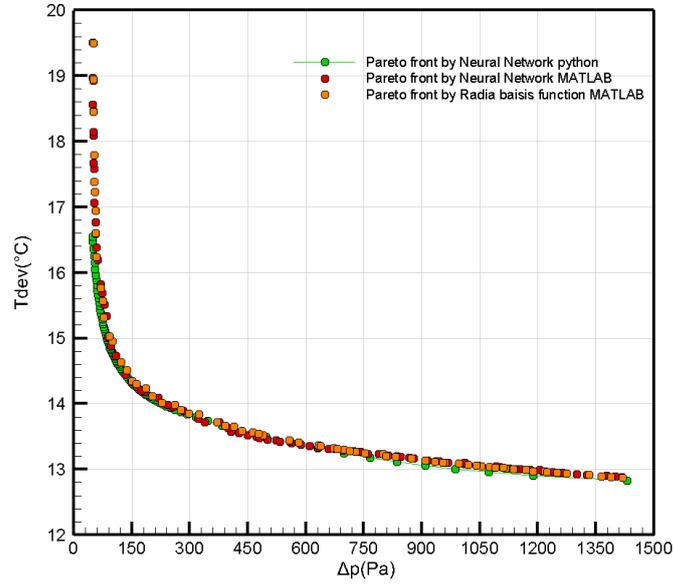
16

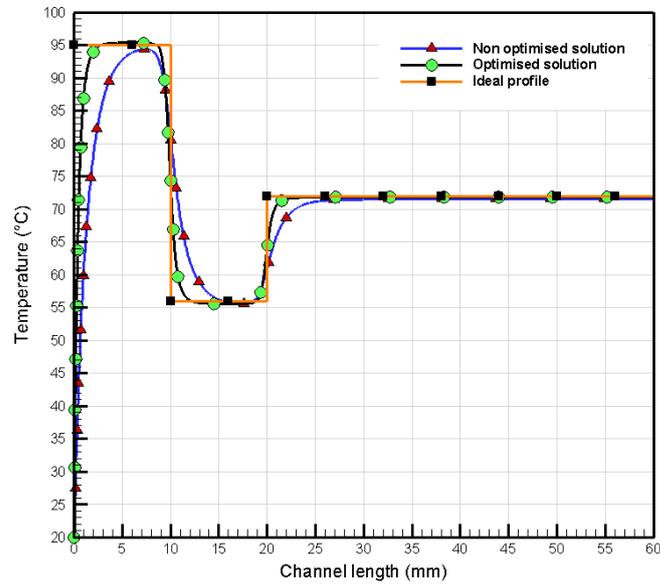Figure 13: Pareto curves of Δp vs T_{dev}, obtained using RBF and NN meta-modelling.

Figure 14: A comparison of temperature profiles in PCR fluidic channel from an optimised and a non-optimised solution.

Figure 15 shows the other two-dimensional Pareto curves for the competing objectives
245 Δp vs Q_t and T_{dev} vs Q_t, obtained using the one-layer NN with 100 neurons available in

17

TensorFlow, combined with the SciPy.optimization module. Figure 15(a) shows that Q_t can be reduced significantly without a major pressure drop penalty, but that reducing it below 0.06 does require a significantly larger Δp. Figure 15(b) shows that there is a reasonably linear, negative correlation between T_{dev} vs Q_t for $T_{dev} > 13$ but that Q_t increases sharply for lower values of T_{dev}.
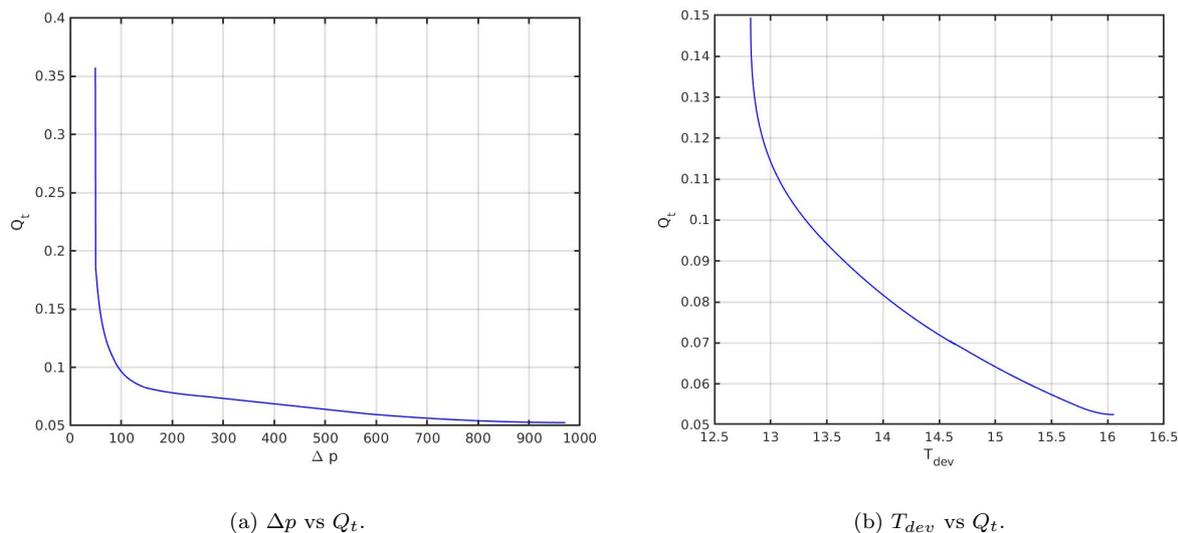

(a) Δp vs Q_t.

(b) T_{dev} vs Q_t.

Figure 15: Pareto curves of the competing objectives.

250

5. Conclusion

This paper proposes the first CFD-enabled optimisation methodology for thermal flow in PCR systems, accounting for temperature uniformity, pressure losses and heating power requirements. Results have shown that temperature variations in the PCR liquid along
255 zones is determined by the competition between convection and conduction in the vertical and axial directions, with the former acting to exacerbate temperature variations and the latter to reduce them. The temperature variations are a nonlinear function of flow rate, channel size, substrate material thermal properties and substrate dimensions. Generally, reducing both the flow rate, which reduces convection, and substrate thermal resistance,
260 $R_{th} = H_b/k_s$, which increases conduction into the liquid, decreases temperature deviations along a channel. The values of the Peclet and axial conduction numbers can provide further, valuable insight into the relative importance of convection and conduction and their influence on temperature uniformity. The dependence of pressure drop and heating power on design variables is much simpler. The former only depends on the channel sizes, W_c and H_c, and
265 increases rapidly as channel cross-sectional area $W_c \times H_c$ decreases, whereas heating power requirements depend mainly on the substrate thermal conductivity, with results showing those for silicon being an order of magnitude larger than for the other materials considered.

If obtaining high levels of temperature uniformity is the key consideration then it is possible to choose a substrate with high conductivity, small substrate thickness and small

18

Acknowledgements:

References

[1] A. D. Stroock, S. K. Dertinger, A. Ajdari, I. Mezić, H. A. Stone, G. M. Whitesides, Chaotic mixer for microchannels, Science 295 (5555) (2002) 647–651.

[2] M. D. Tarn, S. N. Sikora, G. C. Porter, D. O'Sullivan, M. Adams, T. F. Whale, A. D. Harrison, J. Vergara-Temprado, T. W. Wilson, J.-u. Shim, et al., The study of atmospheric ice-nucleating particles via microfluidically generated droplets, Microfluidics and Nanofluidics 22 (5) (2018) 52.

[3] T. Karayiannis, M. Mahmoud, Flow boiling in microchannels: Fundamentals and applications, Applied Thermal Engineering 115 (2017) 1372–1397.

[4] G. Agarwal, T. Kazior, T. Kenny, D. Weinstein, Modeling and analysis for thermal management in gallium nitride HEMTs using microfluidic cooling, Journal of Electronic Packaging 139 (1).

[5] A. F. Al-Neama, N. Kapur, J. Summers, H. M. Thompson, An experimental and numerical investigation of the use of liquid flow in serpentine microchannels for microelectronics cooling, Applied Thermal Engineering 116 (2017) 709–723.

[6] Y. Zhang, H.-R. Jiang, A review on continuous-flow microfluidic PCR in droplets: Advances, challenges and future, Analytica Chimica Acta 914 (2016) 7–16.

[7] X. Zhu, H. Modi, A. Ayala, J. Kilbane, Rapid detection and quantification of microbes related to microbiologically influenced corrosion using quantitative polymerase chain reaction, Corrosion 62 (11) (2006) 950–955.

[8] A. Agrawal, B. Lal, Rapid detection and quantification of bisulfite reductase genes in oil field samples using real-time PCR, FEMS Microbiology Ecology 69 (2) (2009) 301–312.

[9] J. Park, H. Park, Thermal cycling characteristics of a 3d-printed serpentine microchannel for DNA amplification by polymerase chain reaction, Sensors and Actuators A: Physical 268 (2017) 183–187.

[10] J. Lee, M. Lee, E. Kulla, A. Tripathi, The effect of dilution on the dispersion with respect to microfluidic channel geometries, International Journal of Heat and Mass Transfer 104 (2017) 813–818.

[11] J. Khandurina, T. E. McKnight, S. C. Jacobson, L. C. Waters, R. S. Foote, J. M. Ramsey, Integrated system for rapid pcr-based dna analysis in microfluidic devices, Analytical chemistry 72 (13) (2000) 2995–3000.

[12] M. U. Kopp, A. J. De Mello, A. Manz, Chemical amplification: continuous-flow PCR on a chip, Science 280 (5366) (1998) 1046–1048.

[13] S. Thomas, R. L. Orozco, T. Ameel, Thermal gradient continuous-flow PCR: a guide to design, Microfluidics and Nanofluidics 17 (6) (2014) 1039–1051.

[14] J. J. Chen, C. M. Shen, Y. W. Ko, Analytical study of a microfludic DNA amplification chip using water cooling effect, Biomedical Microdevices 15 (2) (2013) 261–278.

[15] P.-C. Chen, W. Fan, T.-K. Hoo, L. C. Z. Chan, Z. Wang, Simulation guided-design of a microfluidic thermal reactor for polymerase chain reaction, Chemical Engineering Research and Design 90 (5) (2012) 591–599.

[16] Q. Cao, M.-C. Kim, C. Klapperich, Plastic microfluidic chip for continuous-flow polymerase chain reaction: Simulations and experiments, Biotechnology journal 6 (2) (2011) 177–184.

[17] M. Hashimoto, P.-C. Chen, M. W. Mitchell, D. E. Nikitopoulos, S. A. Soper, M. C. Murphy, Rapid PCR in a continuous flow device, Lab on a Chip 4 (6) (2004) 638–645.

[18] Y. Schaerli, R. C. Wootton, T. Robinson, V. Stein, C. Dunsby, M. A. Neil, P. M. French, A. J. DeMello, C. Abell, F. Hollfelder, Continuous-flow polymerase chain reaction of single-copy dna in microfluidic microdroplets, Analytical chemistry 81 (1) (2009) 302–306.

[19] M. Mitchell, X. Liu, Y. Bejat, D. Nikitopoulos, S. Soper, M. Murphy, Microfluidics, biomems, and medical microsystems, Proc. SPIE–Int. Soc. Opt. Eng., San Jose, CA, USA.

[20] J. Chiou, P. Matsudaira, A. Sonin, D. Ehrlich, A closed-cycle capillary polymerase chain reaction machine, Analytical chemistry 73 (9) (2001) 2018–2021.

[21] O. Frey, S. Bonneick, A. Hierlemann, J. Lichtenberg, Autonomous microfluidic multi-channel chip for real-time pcr with integrated liquid handling, Biomedical Microdevices 9 (5) (2007) 711–718.

[22] V. Duryodhan, A. Singh, S. G. Singh, A. Agrawal, A simple and novel way of maintaining constant wall temperature in microdevices, Scientific Reports 6 (2016) 18230.

[23] L. Gui, C. L. Ren, Numeric simulation of heat transfer and electrokinetic flow in an electroosmosis-based continuous flow PCR chip, Analytical Chemistry 78 (17) (2006) 6215–6222.

[24] R. Kodzius, K. Xiao, J. Wu, X. Yi, X. Gong, I. G. Foulds, W. Wen, Inhibitory effect of common microfluidic materials on PCR outcome, Sensors and Actuators B: Chemical 161 (1) (2012) 349–358.

[25] Y. Zhang, P. Ozdemir, Microfluidic DNA amplification—a review, Analytica Chimica Acta 638 (2) (2009) 115–125.

[26] V. Miralles, A. Huerre, F. Malloggi, M.-C. Jullien, A review of heating and temperature control in microfluidic systems: techniques and applications, Diagnostics 3 (1) (2013) 33–67.

[27] S. Tsuda, H. Jaffery, D. Doran, M. Hezwani, P. J. Robbins, M. Yoshida, L. Cronin, Customizable 3d printed 'plug and play' millifluidic devices for programmable fluidics, PLoS One 10 (11).

[28] P.-C. Chen, D. E. Nikitopoulos, S. A. Soper, M. C. Murphy, Temperature distribution effects on micro-cfpcr performance, Biomedical Microdevices 10 (2) (2008) 141–152.

[29] D. Moschou, N. Vourdas, G. Kokkoris, G. Papadakis, J. Parthenios, S. Chatzandroulis, A. Tserepi, All-plastic, low-power, disposable, continuous-flow PCR chip with integrated microheaters for rapid DNA amplification, Sensors and Actuators B: Chemical 199 (2014) 470–478.

[30] I. Aziz, R. Jamshaid, T. Zaidiand, I. Akhtar, Numerical simulation of heat transfer to optimize DNA amplification in polymerase chain reaction, in: 2016 13th International Bhurban Conference on Applied Sciences and Technology (IBCAST), IEEE, 2016, pp. 456–462.

[31] D. T. Chiu, A. J. deMello, D. Di Carlo, P. S. Doyle, C. Hansen, R. M. Maceiczyk, R. C. Wootton, Small but perfectly formed? successes, challenges, and opportunities for microfluidics in the chemical and biological sciences, Chem 2 (2) (2017) 201–223.

[32] J. J. Chen, M. H. Liao, K. T. Li, C. M. Shen, One-heater flow-through polymerase chain reaction device by heat pipes cooling, Biomicrofluidics 9 (1) (2015) 014107.

[33] T. L. Bergman, F. P. Incropera, D. P. DeWitt, A. S. Lavine, Fundamentals of heat and mass transfer, John Wiley & Sons, 2011.

[34] J. Holman, Heat transfer, 10th dn (2009).

[35] Y. Cengel, Heat and mass transfer: fundamentals and applications, McGraw-Hill Higher Education, 2014.

[36] J.-R. Lin, C.-M. Wu, T.-M. Liou, C.-Y. Huang, The study of axial heat conduction with various

365   hydraulic diameters of microchannel, Procedia Engineering 79 (2014) 273–278.

[37] G. Maranzana, I. Perry, D. Maillet, Mini-and micro-channels: influence of axial conduction in the walls, International journal of heat and mass transfer 47 (17-18) (2004) 3993–4004.

[38] A. Narayanan, V. Toropov, A. Wood, I. Campean, Simultaneous model building and validation with uniform designs of experiments, Engineering Optimization 39 (5) (2007) 497–512.

370 [39] C. González Niño, N. Kapur, M.-F. King, G. de Boer, A. J. Blacker, R. Bourne, H. Thompson, Computational fluid dynamic enabled design optimisation of miniaturised continuous oscillatory baffled reactors in chemical processing, International Journal of Computational Fluid Dynamics (2019) 1–15.